



UNIVERSITY OF LEEDS

This is a repository copy of *Technical note monitoring the magmas fuelling volcanic eruptions in near-real-time using x-ray micro-computed tomography*.

White Rose Research Online URL for this paper:
<http://eprints.whiterose.ac.uk/80309/>

Version: Accepted Version

Article:

Pankhurst, MJ, Morgan, DJ, Dobson, KJ et al. (4 more authors) (2014) Technical note monitoring the magmas fuelling volcanic eruptions in near-real-time using x-ray micro-computed tomography. *Journal of Petrology*, 55 (3). 671 - 684. ISSN 0022-3530

<https://doi.org/10.1093/petrology/egt079>

Reuse

Unless indicated otherwise, fulltext items are protected by copyright with all rights reserved. The copyright exception in section 29 of the Copyright, Designs and Patents Act 1988 allows the making of a single copy solely for the purpose of non-commercial research or private study within the limits of fair dealing. The publisher or other rights-holder may allow further reproduction and re-use of this version - refer to the White Rose Research Online record for this item. Where records identify the publisher as the copyright holder, users can verify any specific terms of use on the publisher's website.

Takedown

If you consider content in White Rose Research Online to be in breach of UK law, please notify us by emailing eprints@whiterose.ac.uk including the URL of the record and the reason for the withdrawal request.



eprints@whiterose.ac.uk
<https://eprints.whiterose.ac.uk/>

1 **Monitoring the magmas fuelling volcanic eruption in near-real-time**
2 **using X-ray micro-computed tomography.**

3

4 Pankhurst, M. J.^{1*}, Dobson, K. J.^{2,3}, Morgan, D.J. ¹, Loughlin, S.C.⁴, Thordarson,
5 Th.⁵, Lee, P. D. ^{2,3}, Courtois, L. ^{2,3},

6 ¹Institute of Geophysics and Tectonics, School of Earth and Environmental Science, University of
7 Leeds, LS2 9JT, UK

8 ²Manchester X-ray Imaging Facility, School of Materials, The University of Manchester, Oxford Rd.,
9 M13 9PL, UK

10 ³Research Complex at Harwell, Rutherford Appleton Laboratories, Didcot, Oxfordshire, OX11 0FA,
11 UK

12 ⁴British Geological Survey, Edinburgh, EH9 3LA, UK

13 ⁵Institute of Earth Science, University of Iceland, Sæmundargötu 2, 101 Reykjavík, Iceland

14

15 *X-ray micro-computed tomography is here used for the first time to rapidly*
16 *characterize chemical populations of natural olivine crystals. This technique can be*
17 *deployed during volcanic crises, to directly track changes in magma contribution to*
18 *an erupting system in near-real-time. These changes are fundamental to controlling*
19 *the eruption style, duration and intensity. We demonstrate a method that can generate*
20 *data from hundreds of crystals within hours, which allows time-series petrologic data*
21 *to be recorded and interpreted alongside various complimentary monitoring*
22 *techniques (i.e. geophysical approaches). Our direct-detection method broadens our*
23 *view of the dynamic sub-volcanic plumbing system, and provides important insights to*
24 *how an individual eruption may evolve. The same technique can be used to generate*
25 *rich baseline datasets from individual eruption sequences in the rock record in a*
26 *more efficient manner than conventional methods allow.*

27

28 INTRODUCTION

29 Volcanic eruptions are often triggered, sustained, or terminated by changes in
30 magmatic conditions which effect magmatic physical behaviour, such as temperature
31 (T), pressure (P), melt composition including volatile (e.g. H₂O) content (X) and
32 accordant gas and mineral phase stability (Bardintzeff and Bonin, 1987; Cashman,
33 1992; Izbekov et al., 2004; Papale et al., 1998; Pinkerton et al., 2002; Rutherford and
34 Devine, 2003). Mixing between different magmas is frequently implicated as causing
35 these changes: a common scenario is a new pulse entering the sub-volcanic plumbing
36 architecture (Huppert et al., 1982; Sigmundsson et al., 2010; Sparks et al., 1977).
37 Developing capability to detect magmatic changes, understand their influence, and
38 ultimately forecast future eruptive events with high temporal resolution is an ongoing
39 pursuit of volcanologists (Aiuppa et al., 2002; Sparks et al., 2012), due to the
40 enormous capacity for volcanic processes to cause both local (Tanguy, 1994) and
41 global catastrophes (Self, 2006).

42

43 In addition to predicting the beginning of an eruption, other major questions are how
44 large, for how long a duration, and therefore how hazardous could a new eruption
45 become? These forecasts are key to effective planning and crisis management. For
46 instance, in an Icelandic setting, an initial small fissure eruption may have the
47 potential to evolve into a small magnitude 2010 Eyjafjallajökull event (Stevenson et
48 al., 2012), or large magnitude eruptions such as the 1783-1784 AD Laki-type event
49 (Thordarson and Self, 2003). The frequency of explosive eruptions within Iceland and
50 in other settings around the world during historic times, and the large variability in

51 scale they exhibit (Thordarson and Larsen, 2007) strongly suggests these questions
52 will continue to be relevant.

53

54 **The role of igneous petrology in understanding volcanic risk**

55 Igneous petrology provides insights to the magmatic sources and drivers of volcanic
56 processes. The saturation of igneous minerals throughout the evolution of a magma is
57 controlled by the host melt's P, T and X, through time (Wilson, 1989). Cooling
58 magmatic systems evolve from mafic (Mg rich) to felsic (Si rich) in response to
59 precipitation and fractionation of mafic minerals, and the Mg#: $100 \times \text{Mg}/(\text{Mg}+\text{Fe})$ of
60 the residual liquid decreases through time (Villiger et al., 2004). Important
61 physicochemical changes of the magma occur simultaneously with this fractionation
62 and differentiation, such as increases in SiO_2 and/or Al_2O_3 content, increases in
63 volatile concentrations, and changes to crystal type, abundance and chemistry.
64 Concomitant changes in magma viscosity occur throughout this evolution (Giordano
65 et al., 2008). Thus the petrogenesis of erupted products contains evidence of the
66 magmatic parameters through P-T-X space with respect to time, and the chemistry of
67 minerals and melt is a basic proxy for these parameters (Fram and Leshner, 1997; Thy
68 et al., 2006).

69

70 Interaction between batches of magma with different intensive parameters (including
71 P, T, X, crystal and bubble abundance) is a common process (Streck, 2008) that can
72 add further complexity to the overall system as it evolves. Since eruption dynamics
73 are largely controlled by the physicochemical state of the magma (Papale et al., 1998),
74 monitoring such interaction is of great importance. Direct observable consequences of

75 significant magmatic change induced by mixing processes include changes in crystal
76 populations, and crystal chemistry (Sigmarsson et al., 2011).

77

78 **Magmatic change indicated by olivine crystal chemical populations**

79 Olivine in particular can aid identification of deep sources as opposed to shallow
80 sources, for P exerts a strong control on its chemistry (Putirka, 2008). In basaltic-
81 dominated terrains such as Iceland, the olivine chemical population(s) could identify
82 the likely magma source regions and thus differentiate between a large, deep-seated-
83 rift event or small, shallow-remobilised-magma event (Sigmarsson et al., 2011). As
84 such, olivine chemical populations could provide an indication of the eventual scale
85 of a new eruption.

86

87 The composition of olivine lies on a solid-solution between forsterite (Mg_2SiO_4 :
88 denoted as Fo_{100} or $\text{Mg}\#=100$) and fayalite (Fe_2SiO_4 : Fo_0 , $\text{Mg}\#=0$), and the Fe and
89 Mg partitioning between melt and crystal is well understood (Roeder and Emslie,
90 1970). Therefore the Mg# of olivine precipitating from a melt represents a proxy for
91 the stage of differentiation of the equilibrium melt. Hence olivine Mg# populations
92 place important constraints upon local melt conditions and overall magmatic
93 processes (Thomson and MacLennan, 2013).

94

95 Whilst the rim of a growing magmatic olivine crystal reflects the composition of the
96 adjacent melt, each interior is a record of earlier conditions specific to that crystal. A
97 number of processes are identified as contributing crystals to magma. Phenocrysts
98 grew in the magma containing them, antecrysts are earlier precipitates from a discrete
99 but kindred magma/cumulate mush, and xenocrysts are plucked from un-related wall-

100 rock or cumulate-mush (Hildreth and Wilson, 2007; Streck, 2008). Natural magmatic
101 systems can therefore be highly complex, and involve interaction between multiple
102 magmas, each bringing their crystal population and their history to the mix.

103

104 This rich complexity can provide powerful insights to the magmatic system if
105 contributions from individual components can be identified (Kahl et al., 2011). If
106 enough crystals can be analysed to produce statistically robust datasets (Thomson and
107 Maclennan, 2013), changes to magmas and/or contributions from different magmas
108 can be tracked in the erupted crystals throughout the eruption sequence. In this
109 manner, monitoring relative changes to crystal chemical populations in near-real-time
110 are of primary importance.

111

112 **THE PROBLEM**

113 Conventional chemical analysis of crystals requires time intensive preparation. Each
114 mount may take several hours to create (to fully set the resin, which is then ground to
115 expose the grains, and polished to a high quality finish before being carbon coated).
116 Crystals can only be analysed one-at-a-time using Electron Probe Micro-Analysis
117 (EPMA). A few minutes per analytical spot are sufficient to produce quantitative data
118 for major elements and a small number of trace elements. Optimised EPMA and fully
119 quantified electron-dispersive X-ray spectroscopy system set-ups may increase
120 sample throughput, yet necessarily sacrifices precision and the number of elements
121 measured. Even with an optimised system that is based upon an electron beam,
122 material is still required to be mounted in resin, polished and coated. While direct
123 calls have recently been made to monitor eruptive material (Sigmundsson and
124 Hoskuldsson, 2010), and despite the long-recognised advantages of applying

125 petrologic data to volcano monitoring (Devine et al., 1998a; Devine et al., 1998b),
126 rapid high-volume throughput in a time-sensitive situation using standard
127 methodology remains problematic.

128

129 **OUR APPROACH**

130 To overcome this impediment we turn our attention to a far faster method: X-ray
131 micro-computed tomography (XMT; Stock, 1999), and use it to analyse large
132 numbers of entire crystals simultaneously. XMT is a non-destructive density-sensitive
133 imaging method that enables density contrasts to be mapped in 3D. Samples are
134 rotated in an X-ray beam while a high resolution scintillator fronted CCD detector
135 collects images (projections) at different angles. The projections are then
136 “reconstructed” using numerical algorithms to produce a full 3D render of the internal
137 structure of the object (Stock, 1999). Modern laboratory and synchrotron imaging
138 systems can acquire data in as little as a few seconds, at a voxel (the 3D equivalent of
139 a pixel) resolution of $<2\mu\text{m}$. Applications to geological materials prior to our study
140 have focused upon identifying different phases and minerals, and investigating
141 their relationships in static or dynamic 3D (Cnudde and Boone, 2013). Greyscale
142 values can be compared between scans if secondary standards that encompass
143 the X-ray attenuation coefficient of the material of interest, to allow correction
144 for variations in absolute greyscale value that can be caused by fluctuations in X-
145 ray beam current and flux (due to filament age, instrument behaviour etc.)”

146

147 The X-ray linear attenuation coefficient of forsterite and fayalite differ significantly
148 under typical laboratory scan conditions (40-60 kV, Fig. 1). Here we investigate
149 whether a) this difference in attenuation coefficient is sufficient for useful

150 discrimination between olivine crystal compositions, b) whether observed differences
151 can be confidently mapped to measured composition differences and c) how quickly
152 these data can be generated. We have emulated the throughput of samples in a time-
153 sensitive situation, to test how quickly volcano observatories may produce and
154 interpret data during a volcanic crisis. We have used a sample of tephra erupted from
155 the 2010 Fimmvörðuháls flank eruption prior to the Eyjafjallajökull summit eruption,
156 Eastern Volcanic Zone (EVZ) of Iceland, as similar material is most likely to be
157 iteratively sampled during future eruptions.

158

159 **Method applied**

160 Tephra was manually crushed using a steel rolling pin and an aluminum bash-plate
161 before being sieved. 100 grains containing an olivine crystal were picked directly
162 from the 0.5 to 2.0 mm fraction (grains containing whole, intact crystals were
163 preferred), loaded into ~2.0 cm lengths of plastic straw (internal diameter = 4 mm),
164 and capped with pre-prepared resin discs. Three grains containing plagioclase crystals
165 of a similar size as the olivine were added as a control.

166 This experimental charge was then scanned using a Nikon XTH 225ST with a
167 maximum energy of 65 kV using a 1.0 Al filter to minimize beam hardening. This
168 system has a standard static X-ray source and detector (which resolves 2000 x 2000
169 pixels), thus with decreasing distance between the sample and the source, the greater
170 the absolute resolution. The sample rotates around a vertical axis while radiographs
171 (projections) are taken about 360°.

172 Using more projections decreases the number and intensity of reconstruction
173 artefacts, at the expense of time. We found that the balance between data quality
174 and speed of acquisition was optimal at 2000 projections (every 0.18°) per scan.

175 The data were reconstructed using proprietary software to produce a 3D volume
176 containing all 103 grains with a voxel resolution of ~2.5 mm.

177 Digital image processing techniques were used to isolate each olivine crystal using
178 *Aviso* ® and *Fiji*. This involved using pre-existing and freely available plugins to
179 “train” the software to distinguish olivine from plagioclase, glass and air. Once
180 identified, each crystal in the olivine fraction was digitally eroded inwards from
181 the rim by the equivalent of ~15 µm to ensure only the core of the crystals
182 remained. This avoided the sampling of heterogeneous rims -and the attendant
183 potential for error- during subsequent analysis.

184 The average greyscale value of a “spot” of identical size (25 µm radius) was then
185 calculated for each crystal core, excluding obvious inclusions, cracks or zoning. This
186 last step was performed manually in order to ensure a robust dataset with which to
187 compare against future, more sophisticated/automated, image processing methods,
188 and to validate against conventional methods whereby analysis positions are chosen
189 manually. We used standard EPMA techniques to measure the composition of 100
190 olivine crystal cores from the same sample (JEOL 8230, see Appendix for full
191 analytical conditions).

192

193 **RESULTS AND INITIAL CONCLUSIONS**

194 The entire method took <2.5 hours (see figure 2). Total sample preparation time was ~
195 20 min. The scanning and reconstruction steps (image acquisition) were performed
196 in ~30 min each. Image processing (including manual selection) took ~60 min.

197 In our example olivine, plagioclase, glass and air that comprise the 3D volume are
198 easily distinguished by patterns including habit, texture greyscale value. The

199 plagioclase (used as a control) was identified by habit, texture and (low) greyscale
200 value. 13 olivine crystals were discarded due to cracks or inclusions.

201 The reconstructed volume contains olivine crystals with a range of different greyscale
202 values, and often reveals zoning around homogeneous cores (Fig. 2). Thus we show
203 that XMT is capable of resolving even subtle changes in Mg# in natural olivine
204 crystals. A frequency diagram of the greyscale values (n=87) was constructed from
205 both the XMT-spot and EPMA-spot datasets (n=100) using 9 bins (~10% of each n)
206 of equal range (Fig. 3).

207

208 A distinct pattern of greyscale value population frequency is observed, and is matched
209 by the pattern produced by EPMA (Fig. 3). Subtle differences are due to a
210 combination of the non-linear energy dependence of X-ray attenuation coefficient,
211 more pronounced at high Mg#, (see Fig. 1), and two sets of olivine crystals from the
212 same sample. Full EPMA data are reported in the Appendix Table 1, XMT data are
213 reported in Appendix Table 2. Rank-order and linear-array plots of the XMT and
214 EPMA data are provided along with our raw data in the Appendix (Figure 1 and Table
215 3 respectively).

216

217 We find that the XMT method is far faster than standard techniques. The method used
218 has the ability to accurately distinguish chemical populations, which is confirmed by
219 the EPMA data. The use of secondary standards that bracket and intersperse the X-ray
220 attenuation coefficient range of olivine will allow fully comparable data between
221 scans. We conclude that XMT holds great potential to be used as a high-throughput,
222 rapid and accurate method for recording crystal chemical populations, which opens a

223 powerful new avenue of eruption monitoring, and enables the generation of rich
224 baseline datasets.

225

226 **FUTURE APPLICATIONS**

227 To make best use of the suite of olivine crystal applications in a time-critical scenario
228 such as a volcanic eruption, the absolute chemical composition and zonation of
229 olivine crystals must be assessed soon after eruption. Optimised EPMA techniques on
230 polished crystal mounts produces high precision data, but they are time intensive,
231 destructive and limited to 1D and 2D profiles. With appropriate calibration and use of
232 secondary standards, our XMT technique may approach the precision and accuracy of
233 the current methods in terms of chemical composition, and open further avenues for
234 its application in volcanic eruption monitoring.

235

236 For instance, recently developed understanding of solid state Fe-Mg diffusion
237 between zones of different Mg# within olivine has effectively turned zonation profiles
238 in each crystal into a stopwatch of magmatic processes (Costa et al., 2008; Costa and
239 Dungan, 2005; Dohmen and Chakraborty, 2007; Morgan and Blake, 2006). Individual
240 olivine crystals and crystal population dynamics now enhance our view of a sub-
241 volcanic plumbing system through time on a range of scales (Kahl et al., 2011; Kahl
242 et al., 2013). With large enough olivine composition datasets, a detailed picture of
243 magmatic processes feeding alkali basaltic eruptions through time can be resolved,
244 and compared to seismic unrest and deformation signals detected at the surface. This
245 information can aid interpretation of geophysical unrest signals during pre- and syn-
246 eruption events in the future.

247

248 Within alkali basaltic systems such as the active EVZ of Iceland erupted olivine is
249 almost ubiquitous, and displays a variety of crystallisation origins (Passmore et al.,
250 2012). Olivine in these rocks is commonly chemically zoned: generally a
251 homogeneous core is fringed by comparatively narrow zones of different olivine
252 compositions (Thomson and Maclennan, 2013). Systems such as these present prime
253 candidates for XMT-led generation of rich datasets of olivine composition
254 populations and magmatic timescales through eruption sequences. Furthermore,
255 integrating crystal size distributions (CSD) and modal abundances with our qualitative
256 composition approach could be used as a powerful tool in un-tangling magmas and,
257 by extension, understanding crystal-melt relationships. This is because XMT can be
258 used to measure CSD (Jerram et al., 2009), and each crystal can be assigned a unique
259 digital label, allowing large populations of crystals to be characterised by size and
260 composition.

261

262 In the short-term, linking olivine chemical population changes with well-resolved
263 eruption phenomenology (duration, intensity, style) in a forensic manner and merging
264 this with multidisciplinary datasets (Kahl et al., 2013) holds potential to discover
265 important patterns that could be recognized during a future eruption. There is an
266 urgent need for well-documented analysis of past events, since they hold the key to
267 well-constrained pattern recognition. These patterns could be used as empirical lead-
268 indicators of eruptive change, duration and cessation, which are key questions during
269 a volcanic crisis (see Fig. 4). Building this knowledge could be accelerated by using a
270 high-throughput method described here.

271

272 While many hazardous volcanoes are olivine-phyric, many are not. The XMT method
273 is not limited to olivine, for the principles of variable X-ray attenuation coefficient as
274 a proxy for variable composition also applies to many other igneous minerals and
275 glasses. Those with solid-solutions whose end-member compositions represented a
276 large density contrast are particularly suited to this method, such as enstatite-
277 ferrosilite and anorthite-albite. By applying a similar method to other minerals such as
278 orthopyroxene and plagioclase, the XMT technique will be of use in a greater number
279 of volcanic settings. In addition, XMT techniques are not limited to volcanic samples,
280 3D applications to observing compositional patterns in intrusive magmatic rocks and
281 even their sources (i.e. mantle rocks) could hold great value.

282

283 **ACKNOWLEDGEMENTS**

284 The authors wish to thank Dennis Geist, Bruce Marsh and Kate Saunders for their
285 thoughtful reviews of this manuscript, and Marge Wilson and Alastair Lumsden for
286 their editorial roles. MJP, DJM, ThT & SL are supported by NERC grant
287 NE/J024554/1. KJD, LC & PDL wish to acknowledge EPSRC grant EP/I02249X/1,
288 which supports the Manchester X-ray Imaging Facility, and the Research Complex at
289 Harwell. The Faversham is thanked for providing plastic drinking straws for our
290 experimental apparatus. Harri Wyn Williams and Martin Coldwell are thanked for
291 providing sample preparation advice and assistance. The Natural History Museum,
292 London, UK, is thanked for providing mineral specimens used in the proof of concept
293 stage of this work.

294

295 **REFERENCES CITED**

296 Aiuppa, A., Federico, C., Paonita, A., Pecoraino, G., and Valenza, M., 2002, S, Cl and
297 F degassing as an indicator of volcanic dynamics: The 2001 eruption of
298 Mount Etna: *Geophysical Research Letters*, v. 29, no. 11, p. -.
299 Bardintzeff, J.-M., and Bonin, B., 1987, The amphibole effect: A possible
300 mechanism for triggering explosive eruptions: *Journal of Volcanology and*
301 *Geothermal Research*, v. 33, no. 4, p. 255-262.
302 Cashman, K., 1992, Groundmass crystallization of Mount St. Helens dacite, 1980-
303 1986: a tool for interpreting shallow magmatic processes: *Contributions*
304 *to Mineralogy and Petrology*, v. 109, no. 4, p. 431-449.
305 Cnudde, V., and Boone, M. N., 2013, High-resolution X-ray computed tomography
306 in geosciences: A review of the current technology and applications:
307 *Earth-Science Reviews*, v. 123, no. 0, p. 1-17.
308 Costa, F., Dohmen, R., and Chakraborty, S., 2008, Time scales of magmatic
309 processes from modeling the zoning patterns of crystals, *in* Putirka, K. D.,
310 and Tepley, I. F. J., eds., Volume 69, p. 545-594.
311 Costa, F., and Dungan, M., 2005, Short time scales of magmatic assimilation from
312 diffusion modeling of multiple elements in olivine: *Geology*, v. 33, no. 10,
313 p. 837-840.
314 Devine, J. D., Murphy, M. D., Rutherford, M. J., Barclay, J., Sparks, R. S. J., Carroll, M.
315 R., Young, S. R., and Gardner, I. E., 1998a, Petrologic evidence for pre-
316 eruptive pressure-temperature conditions, and recent reheating, of
317 andesitic magma erupting at the Soufriere Hills Volcano, Montserrat, W.I:
318 *Geophysical Research Letters*, v. 25, no. 19, p. 3669-3672.
319 Devine, J. D., Rutherford, M. J., and Gardner, J. E., 1998b, Petrologic determination
320 of ascent rates for the 1995-1997 Soufriere Hills Volcano andesitic
321 magma: *Geophysical Research Letters*, v. 25, no. 19, p. 3673-3676.
322 Dohmen, R., and Chakraborty, S., 2007, Fe-Mg diffusion in olivine II: Point defect
323 chemistry, change of diffusion mechanisms and a model for calculation of
324 diffusion coefficients in natural olivine: *Physics and Chemistry of*
325 *Minerals*, v. 34, no. 6, p. 409-430.
326 Fram, M. S., and Leshner, C. E., 1997, Generation and Polybaric Differentiation of
327 East Greenland Early Tertiary Flood Basalts: *Journal of Petrology*, v. 38,
328 no. 2, p. 231-275.
329 Giordano, D., Russell, J. K., and Dingwell, D. B., 2008, Viscosity of magmatic
330 liquids: A model: *Earth and Planetary Science Letters*, v. 271, no. 1-4, p.
331 123-134.
332 Hildreth, W., and Wilson, C. J. N., 2007, Compositional Zoning of the Bishop Tuff:
333 *Journal of Petrology*, v. 48, no. 5, p. 951-999.
334 Huppert, H. E., Sparks, R. S. J., and Turner, J. S., 1982, Effects of volatiles on mixing
335 in calc-alkaline magma systems: *Nature*, v. 297, no. 5867, p. 554-557.
336 Izbekov, P. E., Eichelberger, J. C., and Ivanov, B. V., 2004, The 1996 Eruption of
337 Karymsky Volcano, Kamchatka: Historical Record of Basaltic
338 Replenishment of an Andesite Reservoir: *Journal of Petrology*, v. 45, no.
339 11, p. 2325-2345.
340 Jerram, D. A., Mock, A., Davis, G. R., Field, M., and Brown, R. J., 2009, 3D crystal
341 size distributions: A case study on quantifying olivine populations in
342 kimberlites: *Lithos*, v. 112, Supplement 1, no. 0, p. 223-235.
343 Kahl, M., Chakraborty, S., Costa, F., and Pompilio, M., 2011, Dynamic plumbing
344 system beneath volcanoes revealed by kinetic modeling, and the

345 connection to monitoring data: An example from Mt. Etna: *Earth and*
346 *Planetary Science Letters*, v. 308, no. 1-2, p. 11-22.

347 Kahl, M., Chakraborty, S., Costa, F., Pompilio, M., Liuzzo, M., and Viccaro, M., 2013,
348 Compositionally zoned crystals and real-time degassing data reveal
349 changes in magma transfer dynamics during the 2006 summit eruptive
350 episodes of Mt. Etna: *Bulletin of Volcanology*, v. 75, no. 2, p. 1-14.

351 Morgan, D. J., and Blake, S., 2006, Magmatic residence times of zoned
352 phenocrysts: Introduction and application of the binary element diffusion
353 modelling (BEDM) technique: *Contributions to Mineralogy and Petrology*,
354 v. 151, no. 1, p. 58-70.

355 Papale, P., Neri, A., and Macedonio, G., 1998, The role of magma composition and
356 water content in explosive eruptions: 1. Conduit ascent dynamics: *Journal*
357 *of Volcanology and Geothermal Research*, v. 87, no. 1-4, p. 75-93.

358 Passmore, E., MacLennan, J., Fitton, G., and Thordarson, T., 2012, Mush
359 Disaggregation in Basaltic Magma Chambers: Evidence from the ad 1783
360 Laki Eruption: *Journal of Petrology*, v. 53, no. 12, p. 2593-2623.

361 Pinkerton, H., Wilson, L., and MacDonald, R., 2002, The transport and eruption of
362 magma from volcanoes: A review: *Contemporary Physics*, v. 43, no. 3, p.
363 197-210.

364 Putirka, K. D., 2008, Thermometers and barometers for volcanic systems:
365 *Reviews in Mineralogy and Geochemistry*, v. 69, no. 1, p. 61-120.

366 Roeder, P. L., and Emslie, R. F., 1970, Olivine-liquid equilibrium: *Contributions to*
367 *Mineralogy and Petrology*, v. 29, no. 4, p. 275-289.

368 Rutherford, M. J., and Devine, J. D., 2003, Magmatic conditions and magma ascent
369 as indicated by hornblende phase equilibria and reactions in the 1995-
370 2002 Soufrière Hills magma: *Journal of Petrology*, v. 44, no. 8, p. 1433-
371 1454.

372 Self, S., 2006, The effects and consequences of very large explosive volcanic
373 eruptions: *Philosophical Transactions of the Royal Society A:*
374 *Mathematical, Physical and Engineering Sciences*, v. 364, no. 1845, p.
375 2073-2097.

376 Sigmarsson, O., Vlastelic, I., Andreasen, R., Bindeman, I., Devidal, J. L., Moune, S.,
377 Keiding, J. K., Larsen, G., Höskuldsson, A., and Thordarson, T. H., 2011,
378 Remobilization of silicic intrusion by mafic magmas during the 2010
379 Eyjafjallajökull eruption: *Solid Earth*, v. 2, no. 2, p. 271-281.

380 Sigmundsson, F., and Hoskuldsson, A., 2010, Develop instruments to monitor
381 volcanic ash fallout: *Nature*, v. 466, no. 7302, p. 28-28.

382 Sigmundsson, F., Hreinsdóttir, S., Hooper, A., Árnadóttir, T., Pedersen, R., Roberts,
383 M. J., Óskarsson, N., Auriac, A., Decriem, J., Einarsson, P., Geirsson, H.,
384 Hensch, M., Ófeigsson, B. G., Sturkell, E., Sveinbjörnsson, H., and Feigl, K. L.,
385 2010, Intrusion triggering of the 2010 Eyjafjallajökull explosive eruption:
386 *Nature*, v. 468, no. 7322, p. 426-432.

387 Sparks, R. S. J., Biggs, J., and Neuberg, J. W., 2012, Monitoring Volcanoes: *Science*,
388 v. 335, p. 1310-1311.

389 Sparks, S. R. J., Sigurdsson, H., and Wilson, L., 1977, Magma mixing: a mechanism
390 for triggering acid explosive eruptions: *Nature*, v. 267, no. 5609, p. 315-
391 318.

392 Stevenson, J. A., Loughlin, S., Rae, C., Thordarson, T., Milodowski, A. E., Gilbert, J.
393 S., Harangi, S., Lukács, R., Hjgaard, B., Árting, U., Pyne-O'Donnell, S.,

- 394 MacLeod, A., Whitney, B., and Cassidy, M., 2012, Distal deposition of
395 tephra from the Eyjafjallajökull 2010 summit eruption: *Journal of*
396 *Geophysical Research B: Solid Earth*, v. 117, no. 6.
- 397 Stock, S. R., 1999, X-ray microtomography of materials: *International Materials*
398 *Reviews*, v. 44, no. 4, p. 141-164.
- 399 Streck, M. J., 2008, Mineral Textures and Zoning as Evidence for Open System
400 Processes: *Reviews in Mineralogy and Geochemistry*, v. 69, no. 1, p. 595-
401 622.
- 402 Tanguy, J. C., 1994, The 1902-1905 eruptions of Montagne Pelée, Martinique:
403 anatomy and retrospection: *Journal of Volcanology and Geothermal*
404 *Research*, v. 60, no. 2, p. 87-107.
- 405 Thomson, A., and Maclennan, J., 2013, The Distribution of Olivine Compositions
406 in Icelandic Basalts and Picrites: *Journal of Petrology*, v. 54, no. 4, p. 745-
407 768.
- 408 Thordarson, T., and Larsen, G., 2007, Volcanism in Iceland in historical time:
409 Volcano types, eruption styles and eruptive history: *Journal of*
410 *Geodynamics*, v. 43, no. 1, p. 118-152.
- 411 Thordarson, T., and Self, S., 2003, Atmospheric and environmental effects of the
412 1783-1784 Laki eruption: A review and reassessment: *Journal of*
413 *Geophysical Research D: Atmospheres*, v. 108, no. 1, p. AAC 7-1 AAC 7-29.
- 414 Thy, P., Leshner, C. E., Nielsen, T. F. D., and Brooks, C. K., 2006, Experimental
415 constraints on the Skaergaard liquid line of descent: *Lithos*, v. 92, no. 1-2,
416 p. 154-180.
- 417 Villiger, S., Ulmer, P., Müntener, O., and Thompson, A. B., 2004, The Liquid Line of
418 Descent of Anhydrous, Mantle-Derived, Tholeiitic Liquids by Fractional
419 and Equilibrium Crystallization—an Experimental Study at 1.0 GPa:
420 *Journal of Petrology*, v. 45, no. 12, p. 2369-2388.
- 421 Wilson, M., 1989, *Igneous Petrogenesis*, Chapman & Hall.

422
423

424 **FIGURE CAPTIONS**

425 **Figure 1.**

426 The dependence of linear attenuation coefficient on X-ray energy for olivine. The
427 linear attenuation coefficient increases with decreasing Mg#. Scanning at lower
428 energies, where the contrast in attenuation coefficient is greatest, results in a wider
429 dynamic range in the reconstructed 3D images. The attenuation coefficient curves for
430 olivine compositions bracketing our samples are shown. The Nikon XTH 225ST
431 laboratory XMT system was run with a polychromatic X-ray beam with a maximum
432 energy of 65kV, and a peak flux at ~40kV.

433 **Figure 2.**

434 XMT workflow for determining olivine crystal composition populations within 2.5
435 hours of sample receipt. Crystals are easily distinguished on the basis of texture and
436 shape. Low-density olivine (high Mg#,) appears darker than higher density olivine
437 (low Mg#). Refinement of the experimental setup may allow faster scanning, and
438 trainable algorithm-based analysis may decrease this workflow time further without
439 sacrificing data quality. Volumes for greyscale value averaging were selected to
440 simulate an EPMA spot, and were placed within the crystal cores, shown
441 schematically as white spots.

442 **Figure 3**

443 Comparison between XMT greyscale value data and EPMA data from olivine crystals
444 in tephra produced during the 2010 Fimmvörðuháls eruption. The XMT data were
445 generated using the XMT workflow described in the text and summarized in Fig. 2. A
446 single EPMA spot was analysed in each crystal core (see the Appendix for full
447 details). The values of each dataset were divided into 9 bins of equal range. The peaks
448 in each population correlate well.

449 **Figure 4**

450 A) Cartoon of hypothetical volcanic behaviour change (observed in real-time), to
451 illustrate a response to major magmatic change within a plumbing system during a
452 protracted eruption. Light shades indicate silicic melts and Fe-rich olivine
453 compositions (i.e. shallow equilibrated, evolved magma), while dark shades indicate
454 Mg-rich compositions (i.e. deeply equilibrated, primitive magma). B) Collection of
455 olivine crystal chemical population histograms stacked through time, corresponding to
456 the processes outlined in A. Such histograms could be generated from erupted
457 material using a workflow similar to ours, allowing insight to magmatic processes at a
458 high temporal resolution. These histograms may be added to the record of event

459 chronology during volcanic eruptions to identify possible correlations with seismic
460 patterns, ground deformation changes and gas monitoring data in near-real-time.
461 Similar plots comprised of data from past eruptions may be used as empirical guides
462 to future volcanism.

463 *Appendix figure and table captions*

464 *Figure 1*

465 Comparison between olivine chemical population data generated by EPMA and XMT
466 from two splits of the same sample of Fimmvörðuháls tephra. a) Decreasing rank
467 order plots of i) 100 EPMA Mg# spots (one in each crystal core) with increasing Mg#,
468 and ii) 87 XMT greyscale value spots (averaged 16-bit greyscale value) with
469 increasing greyscale value. b) Linear array plots of the same data i) EPMA, ii) XMT.
470 Note: higher greyscale values denote brighter voxels = lower Mg#. As such, the XMT
471 linear array order is inverted in b) to allow comparison against Mg#.

472 *Table 1*

473 Electron Probe Microanalysis data from 100 olivine crystal cores from a sample of
474 Fimmvörðuháls tephra, erupted in 2010. Crystals were mounted in resin on a 10x10
475 grid, labelled A-J, 1-10. A 15kV beam at 30nA was used. Elemental abundances were
476 measured against known standards using peak (P) and background (B) counting times
477 as follows: Si P=20s B=10s; Ni P=50s B=25s; Fe P=30s B=15s; Mn P=10s B=5s; Al
478 P=60s B=30s; Ca P=50s B=25s; Ti P=20s B=10s; Mg P=20 B=10s. Mg# =
479 $100 * \text{Mg} / (\text{Mg} + \text{Fe}(t) + \text{Mn})$. Internal standards used were olivine and hematite, which
480 produced compositions within error of long term averages. A linear correction for Fe
481 signal was applied to all analyses, as hematite was used as standard for that element.

482 *Table 2*

483 X-ray micro-computed tomography data from the spots placed on 87 olivine crystal
484 cores from a sample of Fimmvörðuháls tephra, erupted in 2010, as calculated using
485 the workflow detailed in the text, and summarised in figure 2. Each spot was
486 approximately 25 μm in diameter, and 1 voxel deep.

487 *Table 3*

488 Rank-order and linear-array order data used to generate plots displayed in Extended
489 Data Figure 1. Note: higher greyscale values denote lighter voxels = lower Mg#. As
490 such, XMT linear array order is inverted to allow comparison against Mg#.

491 *Table 4*

492 Bins used to generate frequency diagram from XMT greyscale value spots.

Figure 4

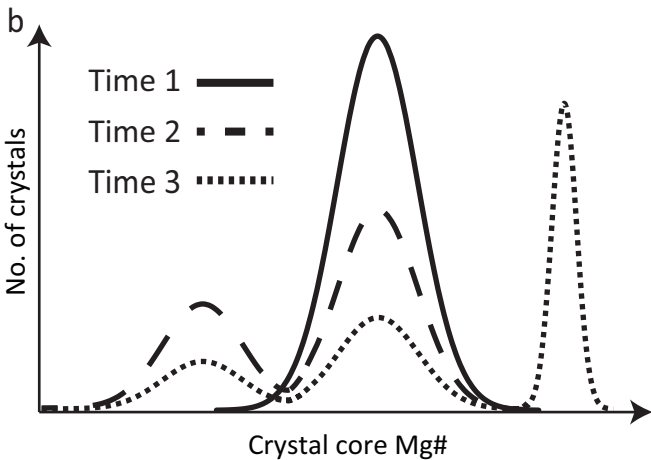
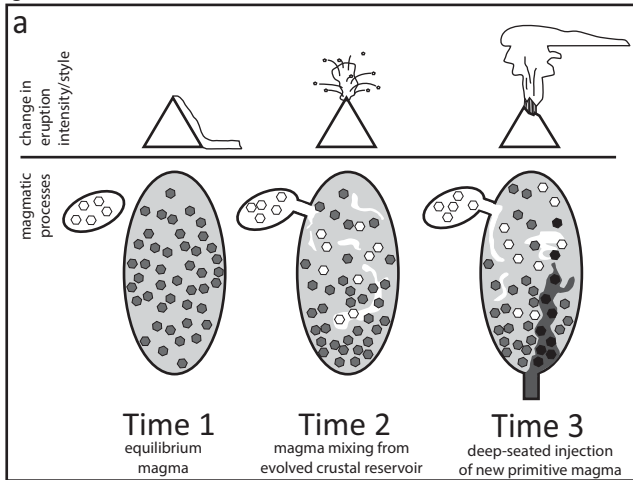


Figure 3

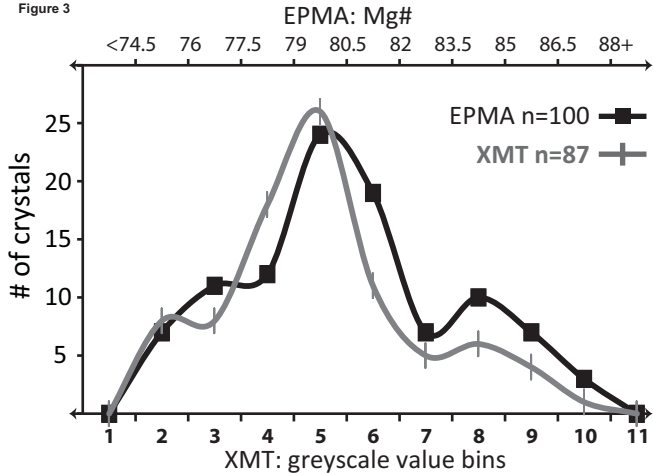


Figure 2

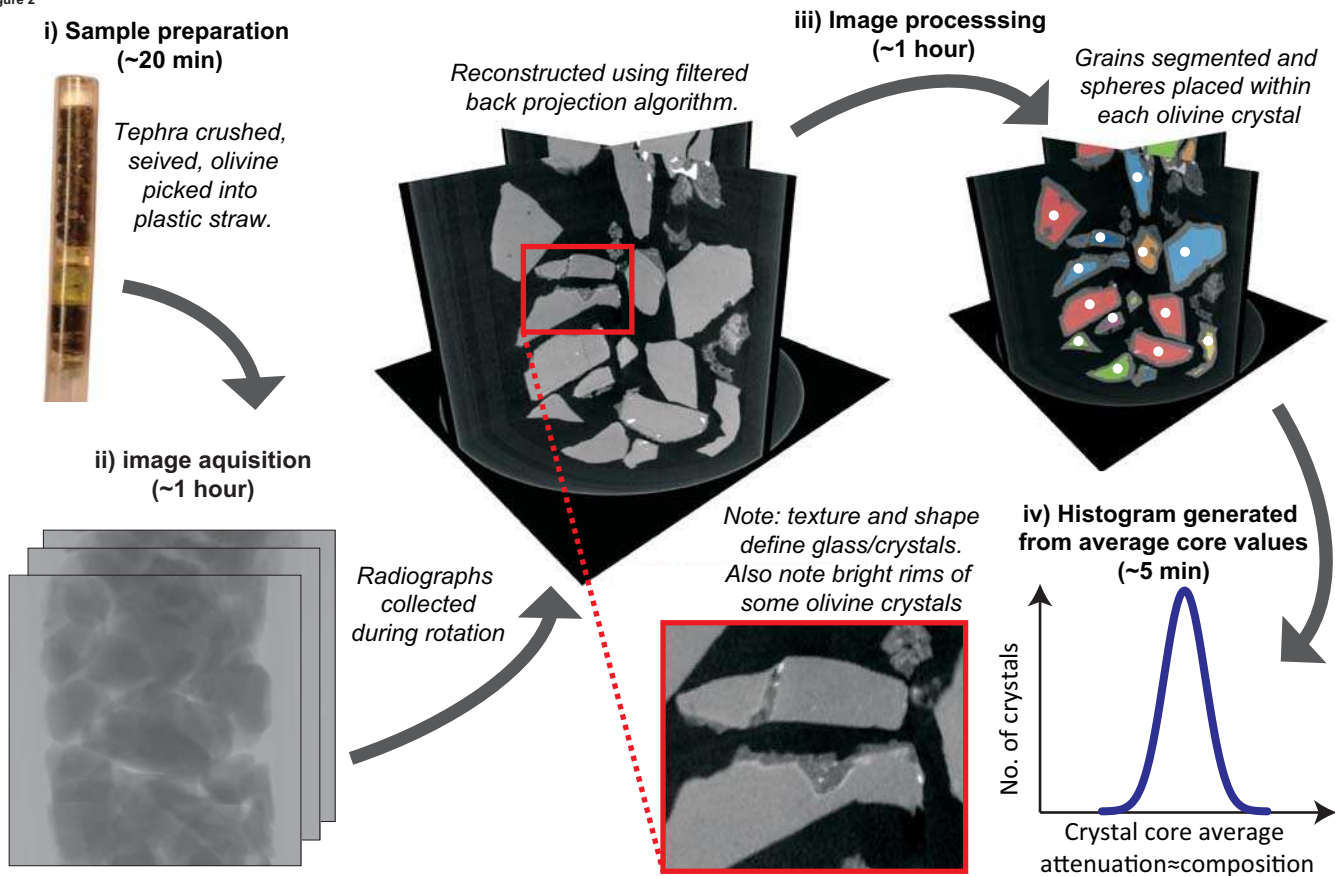
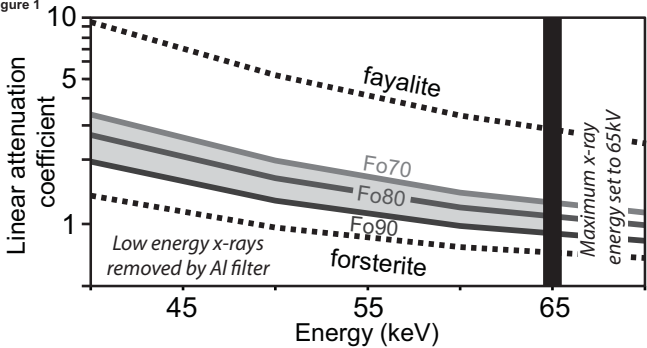


Figure 1



Appendix Table A4. Bins used to generate frequency diagram from XMT greyscale spots

Bin #	Range	
	from	to
1	23550	+
2	23378	23550
3	23206	23378
4	23033	23206
5	22861	23033
6	22689	22861
7	22517	22689
8	22344	22517
9	22172	22344
10	22000	22172
11	-	22000

Appendix Table A3. Rank- and linear array- order of EPMA and XMT data

EPMA data				XMT data			
Mg#	Rank	Linear range	Differential	Average greyscale value	Rank	Linear range	Differential
75.02	100	75.02	0.00	22036.62	87	22037	0
75.22	99	75.15	0.07	22240.40	86	22054	-187
75.53	98	75.27	0.26	22304.52	85	22071	-233
75.63	97	75.40	0.23	22318.63	84	22088	-230
75.76	96	75.52	0.23	22332.52	83	22106	-227
75.96	95	75.65	0.31	22386.92	82	22123	-264
76.00	94	75.77	0.23	22386.94	81	22140	-247
76.07	93	75.90	0.17	22411.09	80	22157	-254
76.25	92	76.02	0.23	22428.06	79	22174	-254
76.48	91	76.15	0.33	22497.01	78	22192	-305
76.79	90	76.27	0.51	22500.18	77	22209	-291
76.80	89	76.40	0.40	22532.20	76	22226	-306
76.84	88	76.52	0.32	22563.31	75	22243	-320
76.85	87	76.64	0.21	22599.51	74	22261	-339
76.89	86	76.77	0.12	22644.19	73	22278	-366
76.95	85	76.89	0.06	22680.95	72	22295	-386
77.17	84	77.02	0.15	22693.69	71	22312	-381
77.23	83	77.14	0.09	22701.87	70	22330	-372
77.73	82	77.27	0.46	22717.55	69	22347	-371
77.74	81	77.39	0.35	22755.27	68	22364	-391
78.08	80	77.52	0.56	22755.69	67	22381	-374
78.21	79	77.64	0.56	22762.92	66	22399	-364
78.22	78	77.77	0.45	22770.07	65	22416	-354
78.31	77	77.89	0.42	22770.12	64	22433	-337
78.38	76	78.02	0.36	22791.85	63	22450	-342
78.58	75	78.14	0.44	22803.65	62	22467	-336
78.61	74	78.27	0.34	22826.04	61	22485	-341
78.66	73	78.39	0.27	22867.06	60	22502	-365
78.69	72	78.52	0.17	22872.01	59	22519	-353
78.77	71	78.64	0.13	22879.71	58	22536	-343
79.20	70	78.77	0.44	22886.65	57	22554	-333
79.21	69	78.89	0.32	22889.91	56	22571	-319
79.43	68	79.01	0.42	22897.38	55	22588	-309
79.56	67	79.14	0.42	22898.13	54	22605	-293
79.67	66	79.26	0.41	22902.99	53	22623	-280
79.69	65	79.39	0.30	22919.73	52	22640	-280
79.74	64	79.51	0.23	22920.37	51	22657	-263
79.75	63	79.64	0.11	22927.86	50	22674	-254
79.75	62	79.76	-0.02	22943.27	49	22691	-252
79.92	61	79.89	0.04	22956.69	48	22709	-248
79.95	60	80.01	-0.06	22964.50	47	22726	-239
80.00	59	80.14	-0.14	22970.34	46	22743	-227
80.05	58	80.26	-0.21	22971.84	45	22760	-211
80.11	57	80.39	-0.28	22977.42	44	22778	-200
80.13	56	80.51	-0.39	22982.00	43	22795	-187
80.13	55	80.64	-0.51	22985.00	42	22812	-173

80.16	54	80.76	-0.60	23000.41	41	22829	-171
80.16	53	80.89	-0.73	23002.69	40	22847	-156
80.17	52	81.01	-0.84	23002.72	39	22864	-139
80.19	51	81.13	-0.95	23007.99	38	22881	-127
80.20	50	81.26	-1.06	23012.22	37	22898	-114
80.31	49	81.38	-1.08	23013.74	36	22916	-98
80.40	48	81.51	-1.11	23017.99	35	22933	-85
80.49	47	81.63	-1.15	23038.58	34	22950	-89
80.55	46	81.76	-1.21	23047.08	33	22967	-80
80.69	45	81.88	-1.20	23052.95	32	22984	-69
80.89	44	82.01	-1.11	23063.83	31	23002	-62
81.06	43	82.13	-1.07	23069.55	30	23019	-51
81.14	42	82.26	-1.12	23069.61	29	23036	-33
81.28	41	82.38	-1.10	23069.73	28	23053	-16
81.29	40	82.51	-1.21	23089.71	27	23071	-19
81.31	39	82.63	-1.32	23089.94	26	23088	-2
81.31	38	82.76	-1.44	23107.06	25	23105	-2
81.38	37	82.88	-1.50	23127.45	24	23122	-5
81.38	36	83.01	-1.62	23132.32	23	23140	7
81.43	35	83.13	-1.70	23133.42	22	23157	23
81.44	34	83.25	-1.82	23136.40	21	23174	38
81.50	33	83.38	-1.88	23149.36	20	23191	42
81.56	32	83.50	-1.95	23152.86	19	23208	56
81.60	31	83.63	-2.03	23173.85	18	23226	52
81.68	30	83.75	-2.08	23183.52	17	23243	59
81.78	29	83.88	-2.10	23210.50	16	23260	50
81.90	28	84.00	-2.11	23211.85	15	23277	66
82.07	27	84.13	-2.06	23212.57	14	23295	82
82.32	26	84.25	-1.93	23217.59	13	23312	94
82.56	25	84.38	-1.82	23230.23	12	23329	99
82.58	24	84.50	-1.92	23254.65	11	23346	92
82.59	23	84.63	-2.04	23260.12	10	23364	103
82.69	22	84.75	-2.07	23310.84	9	23381	70
82.74	21	84.88	-2.13	23425.39	8	23398	-27
83.56	20	85.00	-1.44	23444.72	7	23415	-29
83.88	19	85.13	-1.24	23456.44	6	23433	-24
84.31	18	85.25	-0.94	23467.67	5	23450	-18
84.34	17	85.38	-1.03	23475.56	4	23467	-9
84.37	16	85.50	-1.13	23476.79	3	23484	7
84.40	15	85.62	-1.22	23494.71	2	23501	7
84.46	14	85.75	-1.29	23518.67	1	23519	0
84.52	13	85.87	-1.35				
84.77	12	86.00	-1.23				
84.83	11	86.12	-1.29				
85.03	10	86.25	-1.22				
85.08	9	86.37	-1.30				
85.17	8	86.50	-1.33				
85.35	7	86.62	-1.27				
85.38	6	86.75	-1.37				
85.68	5	86.87	-1.19				
86.41	4	87.00	-0.58				

86.81	3	87.12	-0.31
87.10	2	87.25	-0.14
87.37	1	87.37	0.00

*The differential captures the degree to which each data point (each crystal) departs from a straight line between the highest and lowest value on the corresponding rank order plot, so that comparisons are easier to make visually, see Fig A1.

Appendix Table 2A. XMT averaged greyscale values of crystal core spots.

Crystal	Average greyscale value	Crystal	Average greyscale value
1	22036.62	46	22985.00
2	22240.40	47	23000.41
3	22304.52	48	23002.69
4	22318.63	49	23002.72
5	22332.52	50	23007.99
6	22386.92	51	23012.22
7	22386.94	52	23013.74
8	22411.09	53	23017.99
9	22428.06	54	23038.58
10	22497.01	55	23047.08
11	22500.18	56	23052.95
12	22532.20	57	23063.83
13	22563.31	58	23069.55
14	22599.51	59	23069.61
15	22644.19	60	23069.73
16	22680.95	61	23089.71
17	22693.69	62	23089.94
18	22701.87	63	23107.06
19	22717.55	64	23127.45
20	22755.27	65	23132.32
21	22755.69	66	23133.42
22	22762.92	67	23136.40
23	22770.07	68	23149.36
24	22770.12	69	23152.86
25	22791.85	70	23173.85
26	22803.65	71	23183.52
27	22826.04	72	23210.50
28	22867.06	73	23211.85
29	22872.01	74	23212.57
30	22879.71	75	23217.59
31	22886.65	76	23230.23
32	22889.91	77	23254.65
33	22897.38	78	23260.12
34	22898.13	79	23310.84
35	22902.99	80	23425.39
36	22919.73	81	23444.72
37	22920.37	82	23456.44
38	22927.86	83	23467.67
39	22943.27	84	23475.56
40	22956.69	85	23476.79
41	22964.50	86	23494.71
42	22970.34	87	23518.67
43	22971.84		
44	22977.42		
45	22982.00		

Appendix Table A1. Olivine core compositions measured by EPMA

Crystal	Oxide wt%								total	Mg#
	SiO ₂	TiO ₂	Al ₂ O ₃	FeO	MnO	MgO	CaO	NiO		
FMVDCT_A1a	40.04	0.02	0.05	12.18	0.15	46.71	0.24	0.38	99.77	87.10
FMVDCT_B1	39.76	0.01	0.03	14.56	0.20	44.68	0.23	0.36	99.84	84.37
FMVDCT_C1	38.47	0.02	0.05	21.32	0.31	38.95	0.29	0.14	99.55	76.25
FMVDCT_D1	38.81	0.02	0.04	19.73	0.31	40.61	0.28	0.07	99.87	78.31
FMVDCT_E1	39.43	0.01	0.04	16.59	0.26	42.76	0.24	0.25	99.58	81.90
FMVDCT_F1	38.62	0.04	0.02	20.95	0.31	39.45	0.30	0.14	99.82	76.79
FMVDCT_G1	38.97	0.03	0.03	18.78	0.29	41.32	0.27	0.20	99.89	79.43
FMVDCT_H1	38.80	0.02	0.04	19.42	0.27	40.60	0.30	0.16	99.61	78.61
FMVDCT_I1	38.56	0.02	0.04	20.54	0.33	39.71	0.28	0.10	99.58	77.23
FMVDCT_J1	39.67	0.02	0.05	15.26	0.24	44.18	0.27	0.26	99.93	83.56
FMVDCT_A2	39.40	0.01	0.04	16.08	0.22	43.36	0.24	0.26	99.62	82.59
FMVDCT_B2	38.79	0.03	0.03	19.34	0.29	40.85	0.28	0.12	99.73	78.77
FMVDCT_C2	39.82	0.01	0.05	14.17	0.21	45.12	0.23	0.29	99.90	84.83
FMVDCT_D2	39.77	0.02	0.04	13.87	0.18	45.27	0.26	0.34	99.74	85.17
FMVDCT_E2	38.52	0.03	0.03	20.87	0.33	39.59	0.27	0.13	99.77	76.89
FMVDCT_F2	39.07	0.02	0.02	17.89	0.25	42.00	0.25	0.24	99.73	80.49
FMVDCT_G2	39.09	0.01	0.05	18.15	0.27	41.72	0.24	0.20	99.72	80.16
FMVDCT_H2	39.11	0.02	0.04	18.51	0.28	41.52	0.25	0.19	99.92	79.75
FMVDCT_I2	38.40	0.02	0.03	20.92	0.30	39.41	0.29	0.05	99.41	76.80
FMVDCT_J2	39.28	0.02	0.03	17.22	0.27	42.62	0.26	0.24	99.94	81.28
FMVDCT_A3a	39.06	0.02	0.04	18.45	0.27	41.34	0.26	0.13	99.56	79.74
FMVDCT_B3	39.40	0.01	0.06	16.77	0.26	42.85	0.26	0.23	99.84	81.78
FMVDCT_C3	38.31	0.03	0.03	22.33	0.35	38.23	0.28	0.07	99.63	75.02
FMVDCT_D3	38.92	0.03	0.03	19.34	0.30	40.63	0.27	0.13	99.65	78.66
FMVDCT_E3	38.55	0.01	0.03	21.53	0.29	38.75	0.30	0.05	99.50	76.00
FMVDCT_F3	39.71	0.01	0.04	13.67	0.19	45.42	0.22	0.42	99.69	85.38
FMVDCT_G3	38.37	0.02	0.02	21.52	0.38	39.05	0.27	0.16	99.78	76.07
FMVDCT_H3	39.20	0.03	0.06	17.91	0.27	41.83	0.18	0.17	99.66	80.40
FMVDCT_I3	38.97	0.03	0.04	18.56	0.30	41.45	0.29	0.18	99.82	79.67
FMVDCT_J3	39.26	0.04	0.06	18.20	0.28	41.79	0.27	0.16	100.06	80.13
FMVDCT_A4a	39.60	0.02	0.03	14.98	0.21	44.35	0.24	0.28	99.70	83.88
FMVDCT_B4	39.21	0.02	0.03	18.22	0.26	41.74	0.26	0.15	99.89	80.11
FMVDCT_C4	38.99	0.03	0.03	18.34	0.28	41.59	0.27	0.10	99.64	79.92
FMVDCT_D4	39.35	0.03	0.04	17.00	0.26	42.67	0.25	0.17	99.77	81.50
FMVDCT_E4	39.74	0.01	0.06	13.89	0.22	45.11	0.24	0.30	99.57	85.08
FMVDCT_F4	39.49	0.01	0.04	14.57	0.20	44.50	0.20	0.26	99.27	84.31
FMVDCT_G4	39.19	0.02	0.03	17.77	0.27	41.91	0.27	0.18	99.65	80.55
FMVDCT_I4	39.22	0.02	0.03	17.25	0.28	42.73	0.26	0.22	100.02	81.29
FMVDCT_H4	39.12	0.01	0.03	18.12	0.27	41.75	0.27	0.14	99.71	80.19
FMVDCT_J4	38.86	0.02	0.03	18.92	0.29	41.06	0.28	0.14	99.59	79.21
FMVDCT_A5	38.41	0.02	0.03	21.66	0.35	39.02	0.28	0.10	99.89	75.96
FMVDCT_B5	40.02	0.01	0.05	12.35	0.18	46.23	0.22	0.42	99.48	86.81
FMVDCT_C5a	40.11	0.00	0.06	12.75	0.18	46.15	0.23	0.35	99.84	86.41
FMVDCT_D5	39.25	0.02	0.04	17.07	0.24	42.46	0.25	0.24	99.56	81.38
FMVDCT_E5	39.23	0.02	0.03	17.31	0.27	42.44	0.28	0.17	99.76	81.14
FMVDCT_F5a	39.26	0.02	0.03	17.04	0.30	42.68	0.25	0.17	99.76	81.43
FMVDCT_G5	39.78	0.01	0.07	13.91	0.19	44.95	0.23	0.31	99.45	85.03
FMVDCT_H5a	39.75	0.01	0.06	14.37	0.23	44.73	0.24	0.29	99.69	84.52
FMVDCT_I5	38.84	0.03	0.04	18.18	0.26	41.51	0.25	0.16	99.28	80.05
FMVDCT_J5	38.36	0.03	0.02	21.74	0.38	38.50	0.28	0.09	99.40	75.63
FMVDCT_A6	38.65	0.02	0.05	19.76	0.30	40.07	0.20	0.09	99.13	78.08
FMVDCT_B6	39.09	0.01	0.05	17.09	0.27	42.36	0.24	0.19	99.30	81.31
FMVDCT_C6	39.16	0.02	0.04	16.16	0.25	42.87	0.25	0.21	98.95	82.32
FMVDCT_D6	38.50	0.03	0.02	19.63	0.31	40.14	0.27	0.13	99.02	78.21
FMVDCT_E6	38.23	0.02	0.00	21.59	0.34	38.44	0.26	0.08	98.97	75.76
FMVDCT_F6	39.78	0.03	0.04	14.52	0.20	44.67	0.21	0.31	99.75	84.40
FMVDCT_G6	38.38	0.04	0.02	20.53	0.32	39.54	0.26	0.12	99.21	77.17
FMVDCT_H6	38.96	0.02	0.04	18.10	0.28	41.58	0.27	0.13	99.38	80.13

FMVDCT_I6	39.02	0.02	0.04	17.55	0.26	42.31	0.27	0.22	99.68	80.89
FMVDCT_J6	39.37	0.01	0.04	18.50	0.30	41.38	0.26	0.11	99.97	79.69
FMVDCT_A7	38.32	0.02	0.02	22.11	0.34	38.88	0.26	0.05	100.01	75.53
FMVDCT_B7a	38.85	0.04	0.03	19.36	0.34	40.55	0.25	0.17	99.59	78.58
FMVDCT_C7	38.63	0.02	0.02	20.95	0.30	39.54	0.28	0.13	99.86	76.84
FMVDCT_D7	38.81	0.03	0.03	18.99	0.28	41.16	0.26	0.14	99.69	79.20
FMVDCT_E7	40.05	0.02	0.06	13.45	0.19	45.78	0.25	0.37	100.16	85.68
FMVDCT_F7	38.81	0.02	0.02	20.15	0.32	40.10	0.27	0.17	99.85	77.74
FMVDCT_G7	40.26	0.02	0.05	11.86	0.18	46.72	0.23	0.34	99.64	87.37
FMVDCT_H7	38.86	0.03	0.04	19.70	0.30	40.30	0.28	0.11	99.61	78.22
FMVDCT_I7	39.10	0.00	0.05	18.18	0.26	41.79	0.25	0.15	99.78	80.16
FMVDCT_J7	39.37	0.01	0.06	16.06	0.21	43.77	0.23	0.23	99.94	82.74
FMVDCT_A8	38.68	0.03	0.04	20.25	0.28	40.19	0.28	0.15	99.88	77.73
FMVDCT_B8	39.49	0.02	0.04	17.44	0.26	42.50	0.25	0.26	100.26	81.06
FMVDCT_C8	39.13	0.02	0.03	18.34	0.27	41.77	0.28	0.10	99.95	80.00
FMVDCT_D8	39.28	0.02	0.05	17.12	0.27	42.63	0.25	0.19	99.80	81.38
FMVDCT_E8	38.93	0.04	0.04	19.37	0.28	40.70	0.28	0.11	99.77	78.69
FMVDCT_F8	39.31	0.03	0.03	17.00	0.28	42.99	0.25	0.18	100.06	81.60
FMVDCT_G8	39.08	0.03	0.03	18.32	0.28	41.61	0.27	0.17	99.79	79.95
FMVDCT_H8	38.75	0.02	0.02	19.70	0.30	40.67	0.28	0.12	99.86	78.38
FMVDCT_I8	39.44	0.02	0.04	15.97	0.22	43.37	0.26	0.22	99.54	82.69
FMVDCT_J8	39.60	0.00	0.04	14.47	0.19	44.69	0.24	0.33	99.55	84.46
FMVDCT_A9	39.52	0.01	0.05	14.61	0.20	44.74	0.24	0.30	99.67	84.34
FMVDCT_B9	39.27	0.01	0.03	16.57	0.25	43.20	0.25	0.23	99.81	82.07
FMVDCT_C9	39.05	0.01	0.04	17.72	0.27	42.16	0.26	0.20	99.73	80.69
FMVDCT_D9	39.20	0.02	0.05	17.19	0.25	42.57	0.21	0.19	99.69	81.31
FMVDCT_E9	39.50	0.02	0.04	16.90	0.23	42.84	0.22	0.23	99.99	81.68
FMVDCT_F9	38.30	0.02	0.03	21.07	0.31	39.00	0.28	0.09	99.10	76.48
FMVDCT_G9	38.78	0.03	0.03	20.92	0.28	39.50	0.30	0.03	99.86	76.85
FMVDCT_H9	39.21	0.02	0.02	16.99	0.28	42.51	0.26	0.21	99.50	81.44
FMVDCT_I9	39.18	0.02	0.04	16.94	0.24	42.62	0.23	0.23	99.49	81.56
FMVDCT_J9	39.78	0.01	0.05	13.64	0.19	45.22	0.24	0.29	99.42	85.35
FMVDCT_A10	39.70	0.02	0.05	14.19	0.17	44.85	0.23	0.32	99.52	84.77
FMVDCT_B10	38.94	0.02	0.05	18.76	0.27	41.56	0.21	0.19	100.01	79.56
FMVDCT_C10	39.36	0.01	0.05	18.65	0.26	41.76	0.23	0.12	100.43	79.75
FMVDCT_D10	39.20	0.03	0.04	18.01	0.27	41.82	0.26	0.19	99.82	80.31
FMVDCT_E10	39.02	0.03	0.05	18.13	0.24	41.67	0.24	0.22	99.60	80.17
FMVDCT_F10	39.28	0.03	0.02	16.13	0.23	43.45	0.26	0.28	99.69	82.56
FMVDCT_G10	38.55	0.01	0.02	20.82	0.32	39.59	0.29	0.10	99.71	76.95
FMVDCT_H10	39.07	0.01	0.06	18.12	0.26	41.75	0.23	0.15	99.64	80.20
FMVDCT_I10	39.42	0.01	0.05	16.06	0.25	43.38	0.27	0.30	99.74	82.58
FMVDCT_J10	38.41	0.03	0.03	22.20	0.36	38.42	0.24	0.04	99.74	75.22

Appendix figure 1

